ADVANCED OPTICAL MATERIALS
www.advopticalmat.de

Swift Photochromic Smart Window Based on Plasmonic Yolk-Shell Nanophosphors

Chang Woo Kim, Edgardo Gabriel Santoro, Amol Uttam Pawar, Don Keun Lee, Ovidio Peña-Rodriguez, Umapada Pal, and Young Soo Kang**

Herein, the fabrication of eccentric Ag@Void@Y_2SiO_5:Pr^{3+} plasmonic yolk-shell nanophosphors (PYSNPs) with high up-conversion efficiency, and their incorporation on photochromic WO_3 layers, is demonstrated to fabricate photochromic smart windows with high coloration contrast and swift color change. The up-conversion efficiency of the Pr^{3+} ion-doped Y_2SiO_5 (Y_2SiO_5:Pr^{3+}) nanoshells is enhanced by about 50% through the incorporation of carefully designed plasmonic Ag cores placed inside their hollow cavities. Introduction of these geometry-optimized plasmonic nanophosphors at the surface of photochromic WO_3 films results in about 24-fold and tenfold enhancements of their coloration rate and kinetic constant, respectively. The strategy adopted for designing and fabricating the Ag@Void@Y_2SiO_5:Pr^{3+} PYSNPs and their subsequent incorporation in conventional photochromic films offers an exciting approach for fabricating photochromic smart windows with dynamically controlled transmission of solar radiation, which is a promising technology for reducing energy consumption associated with heating, ventilation, and air-conditioning of buildings.

1. Introduction

About 30% of global energy consumption is attributed to heating and air-conditioning in building systems.[1] Conventional windows used in current buildings are inefficient energy-saving components because a good fraction of energy is lost through them. Indeed, heat gain and loss through windows account for over a quarter of the energy used for heating and cooling.[2–4] To counter this problem, a substantial research effort has been dedicated for developing energy-saving windows, not only for residential and industrial buildings, but also to use them as wavelength-conversion windows in greenhouses and automobiles.[5–8] A smart window should have an energy-saving technology for enhancing lighting and temperature control, maximizing solar gain in winter and minimizing it in summer, simultaneously ensuring the best natural lighting conditions with no glare.[9,10] Hence, all the current technologically-tuned smart windows have some kind of dynamically-modulated switchable optical function, aimed for blocking undesired wavelengths of solar light and passing the desired ones.[11] All of them are based on one of the four stimulus-response mechanisms.[2,3] The electrochromic (EC) windows are constructed by placing electroactive materials between two transparent electrodes, and operated by external electric circuits.[12,13] On the other hand, thermochromic (TC), mechanochromic (MC), and photochromic (PC) windows are made of solid glazing or encapsulations of heat-, strain-, and photo-active materials, respectively.[14,15] The photo-responsive materials in PC smart windows, which are coated over transparent substrates, are the key for wavelength modulation under solar light irradiation.[16–19] While sunlight is the unique requirement for operating PC smart windows, their practical application demands a high coloration contrast, fast reversible switching speed and high photochemical stability of PC materials.

Organic materials have been widely utilized in PC smart windows, and investigated to highlight the principles of photochromism, bleaching, and color change. However, most of these organic PC materials, with the exception of naphthopyran, have the serious drawback of irreversible color change at initial stage during the process of blocking and passing the light.[2,4] Such shortcoming restricts their application as smart window materials and forced the researchers to turn-on to inorganic PC materials for reversible switching. Photochromism in switchable PC windows is derived by the color change for selective visible light transmittance, which is accompanied by reversible

C. W. Kim
Department of Nanotechnology Engineering
College of Engineering
Pukyong National University
Busan 48513, Republic of Korea
E. G. Santoro, A. U. Pawar, D. K. Lee, Y. S. Kang
Environmental and Climate Technology
Korea Institute of Energy Technology (KENTECH)
Naju-Si, Jeollanam-do 58219, Republic of Korea
E-mail: yskang@kentech.ac.kr
O. Peña-Rodriguez
Instituto de Fusión Nuclear "Guillermo Velarde"
Universidad Politécnica de Madrid
José Gutiérrez Abascal 2, Madrid E-28006, Spain
U. Pal
Instituto of Physics
Autonomous University of Puebla
P.O. Box J-48, Puebla 7257, Mexico
E-mail: upal@ifuap.buap.mx
The ORCID identification number(s) for the author(s) of this article can be found under https://doi.org/10.1002/adom.202202171.

DOI: 10.1002/adom.202202171

change in different thermodynamic energy levels of their molecular structures or oxidation states of constituting elements.[20] Generally, the photochromic phosphotungstic acid ($H_3PW_{12}O_{40}$, HPW), one of the polyoxometalate compounds, changes reversibly from colorless to brownish-blue and back under UV and visible light irradiation, respectively.[18,21] Its photochromic properties are induced by the reduction of W^{6+} ion to W^{5+} through charge transfer from oxygen to the metal under UV exposure.[21] As a smart window component, HPW films have the advantage that they can control the intensity of transmitted visible light via coloration density change produced by the absorption of UV light.[22,23] However, the utilization of HPW in smart windows is severely restricted, as the contribution of UV light is barely ~5% in the standard AM 1.5G solar spectrum. Although a vast amount of research (both theoretical and experimental) has been performed on the design and fabrication of efficient nanophosphors and photochromic materials to overcome this restriction, the problem is far from solved. Previously, we demonstrated that the photo-response and energy conversion efficiency of a phosphor film can be enhanced through structural engineering.[20,24,25] Therefore, understanding the nature of interfacial structure of hybrid nanophosphors at atomic and molecular levels during photo-conversion process is critical to design efficient photo-conversion devices, like smart windows. Utilization of engineered nano- and micro-structures of photochromogenic materials with high up-conversion efficiency can compensate the deficiency associated to the low UV fraction in solar light.

Here, we present a novel approach for fabricating photochromic smart windows with high coloration contrast and fast color switching, integrating plasmonic yolk-shell nanophosphors (PYSNPs) at the surface of photochromic layers. By adjusting the geometrical parameters, that is, the size of plasmonic yolk, its position in the cavity of phosphor shell and the thickness of phosphor shell, we could fabricate Ag@Void@Y_2SiO_5:Pr^{3+} nanophosphors with about 50% higher up-conversion efficiency, compared to non-plasmonic Y_2SiO_5:Pr^{3+} nanophosphors. The optimized design of the PYSNPs allowed us to fabricate intelligent photochromic smart windows with swift coloration ability. The photochromic smart windows fabricated with WO_3 photochromic layer coupled with PYSNPs exhibited considerable improvements in coloration rate and kinetic constant. The strategy adopted in the design and fabrication of plasmonic up-conversion nanophosphor will open up the possibility of developing new super-luminescent nanophosphors and intelligent fast switchable photochromic smart windows.

2. Results and Discussion

2.1. Optical Response of Yolk-Shell Structures

Tremendous efforts have been devoted recently to fabricate efficient wavelength conversion films for applying them in smart windows.[2,26,27] To achieve this goal, we optimized the geometry of plasmonic nanophosphors with yolk-shell configuration by adjusting the size of plasmonic Ag core, phosphor shell thickness and the hollow space between them. The PYSNPs were fabricated via a tailored three-step process: i) Synthesis of Ag core nanoparticles, ii) sequential shell formation, and iii) after-growth heat treatment to form the void between the plasmonic nanoparticle and the nanophosphor shell (**Figure 1**). The optimized PYSNPs (Figure S1, Supporting Information) were used to fabricate PC window films, to test their performance as swift color-switching smart windows in realistic conditions.

To fabricate the PYSNPs, first we synthesized the silver nanoparticles by Turkevich method.[28] Silver nanoparticles of four different sizes (10, 40, 80, and 120 nm diameters) were fabricated to tune the localized surface plasmon resonance (LSPR) wavelength of the plasmonic PYSNPs close to the maximum of the solar spectrum (Figure S2, Supporting Information).

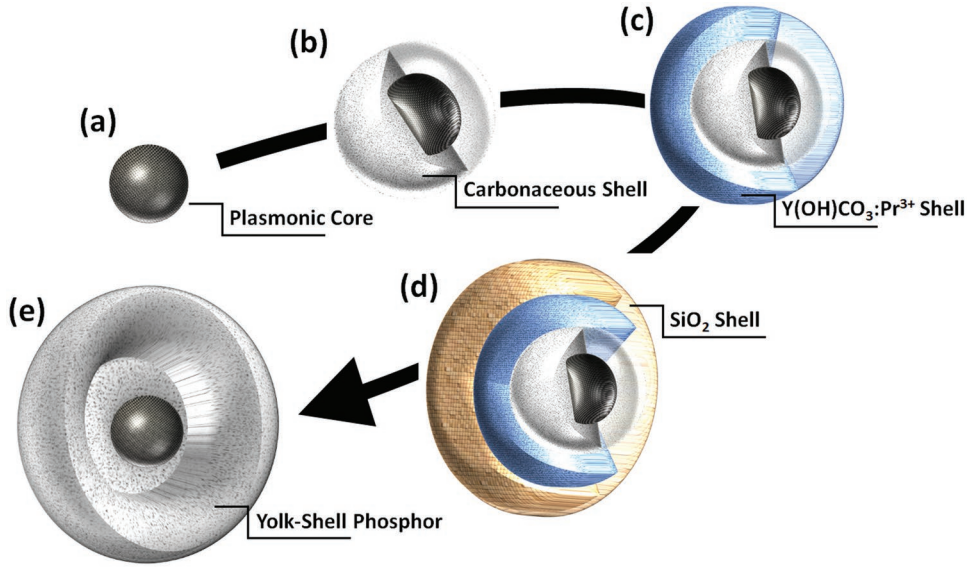

Figure 1. Schematic illustration of plasmon-mediated yolk-shell phosphor particles produced through sequential shell formation using wet-chemical process.

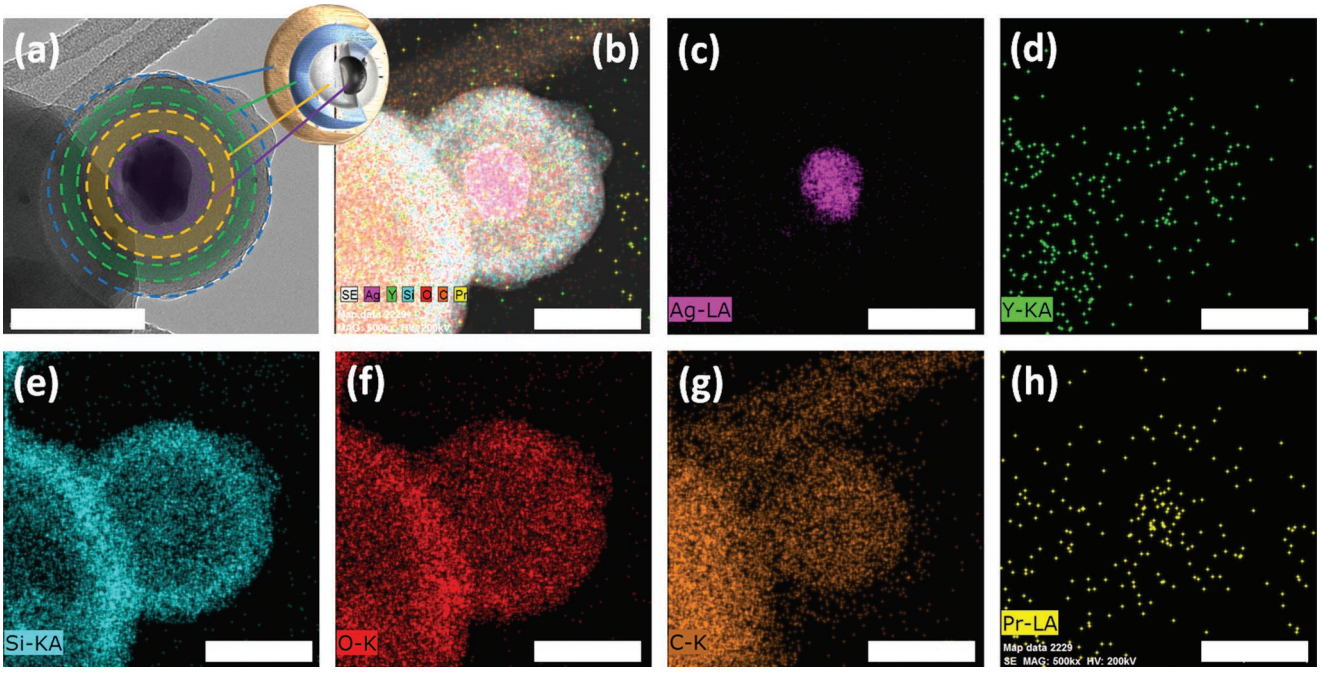

Figure 2. Transmission electron microscopy (TEM) and elemental mapping. a) A typical TEM image and b–h) EDS elemental mapping images of Ag@C@Y(OH)CO_3:Pr^{3+}@SiO_2 structures prepared by sequential shell formation, showing: b) all the studied elements, c) Ag, d) Y, e) Si, f) O, g) C, and h) Pr. White bars in the images represent 100 nm.

All the Ag NPs were crystalline, grown in face-centered-cubic phase (Figure S2, Supporting Information), and manifested strong characteristic LSPR absorption bands (Figure S3, Supporting Information). Hereafter, they will be designated as $_{10}$Ag (16.0 ± 4.5 nm average size), $_{40}$Ag (46.0 ± 8.0 nm average size), $_{80}$Ag (75.0 ± 15.0 nm average size), and $_{120}$Ag (120.0 ± 30.0 nm average size).

The as-prepared Ag nanoparticles were then encapsulated by carbonaceous shells of different thicknesses (10–160 nm) that served as templates for fabricating the final hollow PYSNPs with different inner void spaces. As can be seen in Figure S4, Supporting Information, all the Ag@C core-shell nanoparticles of different core sizes and shell thicknesses maintained their spherical morphology. For the fabrication of Y_2SiO_5:Pr^{3+} (YSO:Pr^{3+}) shells, Y(OH)CO_3:Pr^{3+}, and SiO_2 layers were sequentially formed over the prefabricated Ag@C particles (Figure S5, Supporting Information). Transmission electron microscopy observation and elemental mapping of individual spherical particles confirmed the formation of multi-layered shells and desired element-distribution in the as-grown yolk-shell structures (**Figure 2**).

The final Ag@Y_2SiO_5:Pr^{3+} yolk-shell structures were obtained by annealing the Ag@C@Y(OH)CO_3:Pr^{3+}@SiO_2 particles at 1000 °C in air for 3 h, which induced the Kirkendall effect[29] for the inter-diffusion of the elements between the Y(OH)CO_3:Pr^{3+} and SiO_2 shell layers and removed the carbonaceous shell around the Ag particles. The size of individual composite particles and hollow space between Ag core and YSO:Pr^{3+} shell was reduced due to thermal shrinkage by the Kirkendall effect, maintaining their original spherical morphology (Figure S6, Supporting Information). Energy dispersive spectroscopy analysis in transmission electron microscope (TEM) revealed a homogenous distribution of Y, Si, O, and Pr elements in the shell layers of the yolk-shell Ag@YSO:Pr^{3+} nanophosphors. Likewise, silver remained as a small core particle inside the structure (Figure S6, Supporting Information). A complete removal of carbon template from the final PYSNPs could be confirmed by comparing the elemental mapping images of the nanostructures before and after calcination.

The final size of the PYSNPs with Ag@Void@YSO:Pr^{3+} configuration could be controlled from 110 to 300 nm, with D_{Ag}@D_{Void}@D_{YSO} of 20 nm@60 nm@110 nm (Figure S7, Supporting Information), 35 nm@95 nm@300 nm (Figure S8, Supporting Information), 40 nm@120 nm@230 nm (Figure S9, Supporting Information), and 40 nm@100 nm@300 nm (Figure S10, Supporting Information). To elucidate the effect of LSPR in yolk-shell nanophosphors, we also synthesized pristine hollow YSO:Pr^{3+} phosphor particles (i.e., without Ag nanocore) of about 200 nm diameters (Figure S11, Supporting Information). X-ray diffraction (XRD) pattern of the pristine hollow YSO:Pr^{3+} particles (Figure S12, Supporting Information) revealed their monoclinic crystalline phase (PDF# 52–1810), whereas the Ag@YSO:Pr^{3+} PYSNPs fabricated with Ag cores of different sizes exhibited two additional diffraction peaks around 38.11° and 77°, due to the presence of metallic silver nanoparticles (PDF# 65–2871).

To study the influence of the yolk-shell configuration over the optical properties of the nanostructures, we performed finite differences in the time domain (FDTD) simulations (Figure S13, Supporting Information, for details see Section 4). The calculations were performed for several structures, and they all exhibit a similar behavior, which is more pronounced for the structure with dimensions (D_{Ag}@D_{Void}@D_{YSO}) of 40 nm@80 nm@220 nm. Calculated far-field and near-field

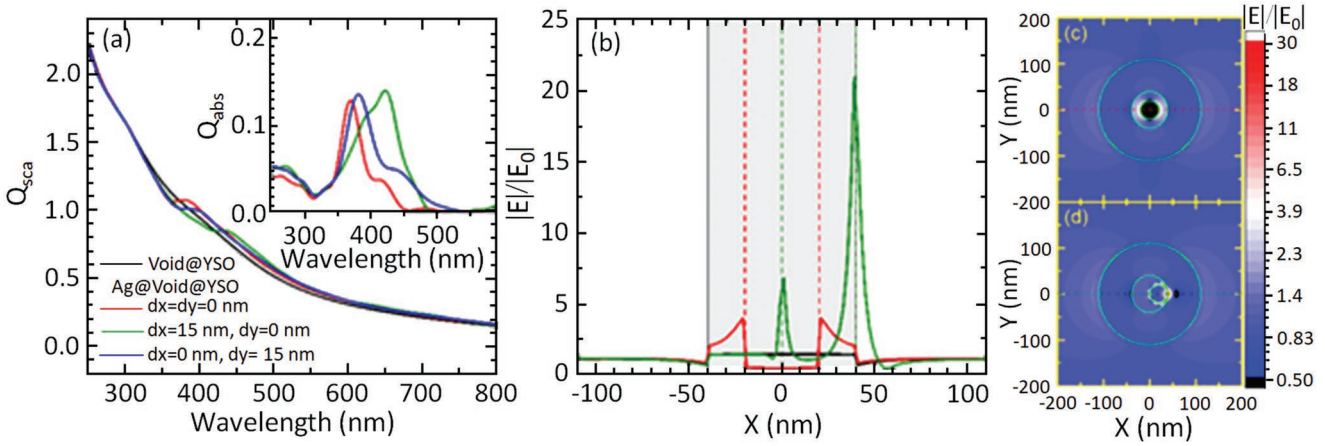

Figure 3. a) Scattering efficiency, b) electric field enhancement along the displacement axis for Void@YSO and Ag@Void@YSO structures, and maps of electric field for c) concentric and d) eccentric Ag@Void@YSO structures. The inset in (a) represents the absorption efficiency for the same structures. The dark area in (b) represents the void and vertical dashed lines the concentric (red) and eccentric (green) core.

distributions for this PYSNP are depicted in **Figure 3**. The far-field (Figure 3a) is heavily dominated by the contribution of the YSO shell. This is particularly evident in the large value of the scattering efficiency, which is barely affected by the introduction of the silver core (irrespective of its location). Moreover, the presence of Ag core hardly affects the absorption efficiency of the hybrid structures (inset of Figure 3a), which increases only to about 0.1 with the introduction of the metallic core. On the contrary, silver core has a huge effect on the near-field (Figure 3b–d). For the concentric core, most of the enhancement occurs in the void, which is not useful to enhance the up-conversion of the phosphor shell. However, the electric field increases about one order of magnitude when the core is displaced to an eccentric position and, more importantly, a sizable part of this enhancement occurs inside the YSO layer (Figure 3b,c). Undoubtedly, this effect can contribute to improve the up-conversion efficiency of the PYSNPs.

On introducing a silver core inside the YSO:Pr^{3+} shell, the overall up-conversion rate of the nanophosphor is controlled by two different processes. In the first one, the visible light absorbed by the phosphor shell layer is directly up-converted to UV light (Figure S14, Supporting Information). Hence, we will refer this as the direct up-conversion process. In addition, the fraction of incident (excitation) light transmitted through the phosphor shell layer reaches the Ag core, which absorbs it. The intense electric field produced around the silver core at the plasmon wavelength can transfer a part of the energy absorbed by the LSPR to the phosphor layers of the hybrid nanostructures. Pumping of such selective energy (through enhancement of electric field inside the PYSNPs), which is the most appropriate excitation energy of the phosphor, enhances its up-conversion efficiency (Figure S14, Supporting Information). We designate this as the plasmon-assisted up-conversion process. However, the presence of the metallic core can also increase the non-radiative decay due to energy transfer from the phosphor to the silver particle, quenching the direct up-conversion in the YSO shell.[30] This effect can be aggravated by the core eccentricity. The influence of the separation between the silver core and the YSO shell can be quantified with the equations reported by Bharadwaj and Novotny:[31]

$$\frac{\gamma_{em}}{\gamma_{em}^0} = \frac{\gamma_{exc}}{\gamma_{exc}^0}\frac{q}{q^0} \tag{1}$$

$$\frac{\gamma_{exc}}{\gamma_{exc}^0} = \left|1+2\frac{a^3}{(a+z)^3}\frac{\varepsilon(\omega_2)-1}{\varepsilon(\omega_2)+2}\right|^2 \tag{2}$$

$$q = \frac{\gamma_r/\gamma_r^0}{\gamma_r/\gamma_r^0+\gamma_{abs}/\gamma_r^0+\left(1-q^0\right)/q^0} \tag{3}$$

$$\frac{\gamma_r}{\gamma_r^0} = \left|1+2\frac{a^3}{(a+z)^3}\frac{\varepsilon(\omega_2)-1}{\varepsilon(\omega_2)+2}\right|^2 \tag{4}$$

$$\frac{\gamma_{abs}}{\gamma_r^0} = \frac{3}{16}\mathrm{Im}\frac{\varepsilon(\omega_2)-1}{\varepsilon(\omega_2)+1}\frac{1}{k_2^3 z^3}\frac{\left(p_x^2+p_y^2+2p_z^2\right)}{|\mathbf{p}|^2} \tag{5}$$

where the superscript "0" refers to the quantity in the absence of LSPR enhancement. γ_{em}, γ_{exc}, and γ_r are, respectively, the emission, excitation, and radiative decay rates of the phosphor. γ_{abs} is the non-radiative decay rate, associated to energy transfer from the phosphor to the Ag core. q is the quantum yield, a is the Ag core radius, z is the distance between Ag core and phosphor shell, $\varepsilon(\omega_2)$ is the dielectric constant of Ag as a function of dipole frequency, $k = 2\pi/\lambda$ is the wave vector ((λ is the wavelength of light), and $p = [p_x,p_y,p_z]$ is the dipole moment. It should be noted that Equations (2) and (4) are identical because the dipole is assumed to be oriented along a Cartesian axis.[31]

Using Equations (1–5), we calculated the emission enhancement for a silver nanoparticle of 20 nm radius, at two different wavelengths, 300 and 488 nm, with dielectric functions equal to 0.83987 + i2.6498 and − 9.1226 + i0.30208, respectively.[32] In this way, we can compare the differences in enhancement below and around the LSPR position. For simplicity, we assumed a dipole orientation that makes $p_x = p_y = 0$, and a high intrinsic quantum yield: $q^0 = 1$. The calculated emission enhancement

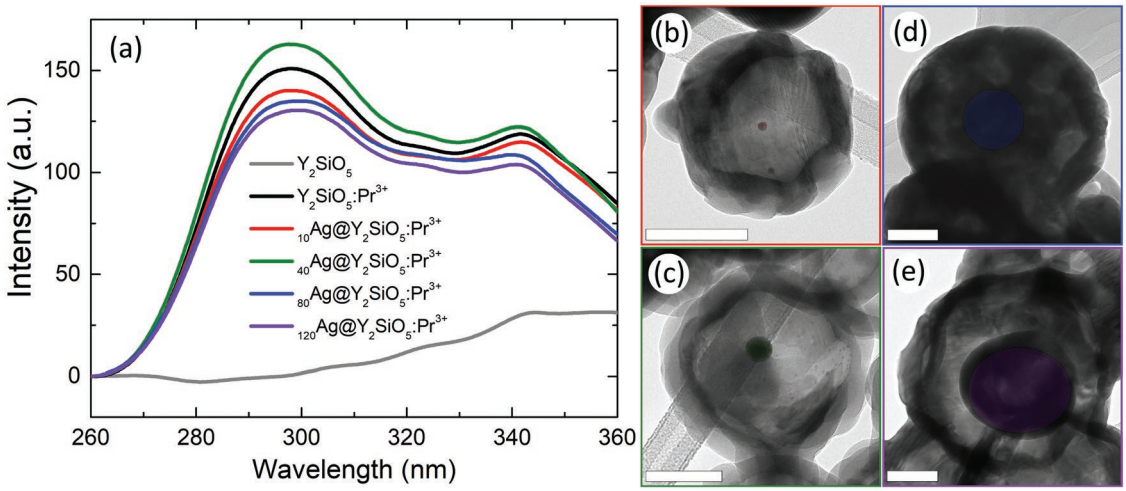

Figure 4. a) Core size dependent emission spectra of yolk-shell nanostructures under 488 nm excitation, and corresponding TEM images with Ag cores having sizes of b) 10 nm, c) 40 nm, d) 80 nm, and e) 120 nm. Silver cores have been highlighted with their respective colors, to facilitate identification. White bars in TEM images represent 100 nm.

is depicted in Figure S15, Supporting Information, as a function of the separation between the metallic nanoparticle and the phosphor shell (z). It can be seen that around the LSPR wavelength, the emission enhancement is dominant over most of the distances (the quenching is dominant only below 3 nm). Hence, it is expected that the eccentric cores should greatly enhance the up-conversion of the phosphor shell. On the other hand, far from the LSPR wavelength, the quenching is dominant for all of the distances, which highlights the importance of tuning the LSPR to match the excitation wavelength.

The up-converted UV light emission intensities of the YSO nanoshells with and without Pr^{3+} were compared with the UV light emission intensity of the PYSNPs (**Figure 4**). The up-conversion behavior of the PYSNPs was analyzed by measuring their emission spectra in the 260–360 nm range under 488 nm excitation, which corresponds to the main absorption wavelength of the YSO:Pr^{3+} nanophosphor (Figure 4). The hollow YSO structures without Pr^{3+} ions did not reveal any characteristic emission peak or up-conversion behavior under 488 nm excitation, as expected. However, the pristine hollow YSO:Pr^{3+} particles revealed a strong emission band in the 280–290 nm spectral range, which corresponds to the 4f 5d → 3Hj interband transition of Pr^{3+} ions. An additional emission band of lower intensity was also detected between 320 and 360 nm, which corresponds to the 4f 5d → 3Fj multiplet (Figure S16, Supporting Information), a characteristic emission of YSO:Pr^{3+} produced by up-conversion.[20,33]

Figure 4 also depicts the emission spectra of Ag@Void@YSO:Pr^{3+} PYSNPs, all of about 200 nm sizes, illustrating the effect of core size on the up-conversion process. Interestingly, the up-conversion emission of the $_{40}$Ag@YSO:Pr^{3+} PYSNPs was the most intense among all the fabricated PYSNPs, with an emission intensity enhancement of about 5.8%, compared to the emission intensity of the hollow pristine YSO:Pr^{3+} phosphor. On the other hand, the emission intensities of the $_{10}$Ag@YSO:Pr^{3+}, $_{80}$Ag@YSO:Pr^{3+}, and $_{120}$Ag@YSO:Pr^{3+} PYSNPs were about 4.76%, 8.42%, and 12.13% lower than the emission intensity of the hollow pristine YSO:Pr^{3+} nanophosphor, respectively. The observed variation in the emission intensity of the PYSNPs can be explained by the two competing effects that affect plasmon-assisted up-conversion. On exciting the PYSNPs with 488 nm wavelength, which is close to the LSPR maximum of the $_{40}$Ag nanocores, the enhancement of UV emission of the $_{40}$Ag@YSO:Pr^{3+} yolk-shell dominates over the quenching. On the contrary, the maximum of the plasmon band for $_{10}$Ag is located around 405 nm (Figure S3, Supporting Information) with narrow peak width, which means that the silver plasmon cannot be properly excited by the 488 nm wavelength. Hence, the quenching process is dominant, worsening the overall emission intensity. The same applies to the $_{80}$Ag and $_{120}$Ag plasmonic nanocores, probably even aggravated by their larger sizes and non-spherical morphology, that results in broader LSPR peaks with lower intensity (Figure S3, Supporting Information). A smaller separation between plasmonic core and phosphor shell layer, along with eccentric location of metal core in the hollow space might also contribute to increase the quenching.[30]

To understand the effect of the intermediate void on the up-conversion behavior of PYSNPs, four $_{40}$Ag@YSO:Pr^{3+} samples with different diameters of the hollow YSO:Pr^{3+} shells were prepared utilizing prefabricated $_{40}$Ag@C nanostructures with different carbon shell thicknesses. The diameters of the hollow space in the PYSNPs were adjusted to 60, 120, 160, and 240 nm, with overall average size of Ag@YSO:Pr^{3+} structures between 220 and 330 nm (**Figure 5**). As can be noticed in Figure 5, in comparison with the pristine hollow YSO:Pr^{3+} nanoparticles (Figure 4), the up-converted UV emission intensity of the $_{40}$Ag@YSO:Pr^{3+} nanostructures with hollow space diameters of 120, 160, and 240 nm increased by 23.1%, 19.9%, and 5.8%, respectively. The $_{40}$Ag@YSO:Pr^{3+} PYSNPs with a void diameter of 60 nm produced the highest up-conversion enhancement of 45.1%.

As we have discussed, the fraction of incident light reaching the Ag core depends on the light transmitted through the external shell layer. Consequently, the up-conversion efficiency of the hybrid phosphor particles also depends on the

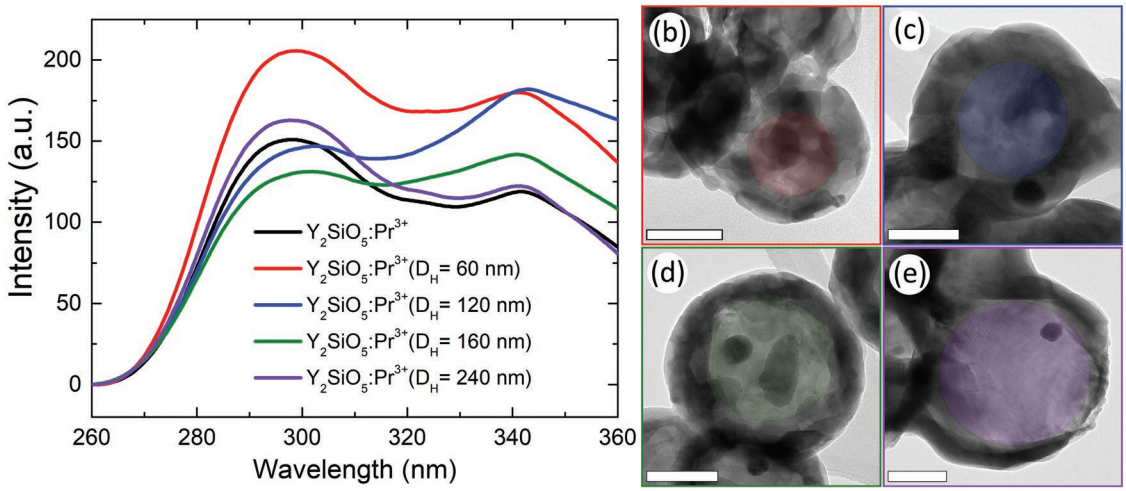

Figure 5. a) Emission spectra at 488 nm excitation, and TEM images of $_{40}$Ag@YSO:Pr^{3+} yolk-shell nanostructures of different hollow space dimensions: b) 60 nm (red), c) 120 nm (blue), d) 160 nm (green), and e) 240 nm (violet) of hollow diameter. Voids have been highlighted with their respective colors, to facilitate identification. White bars in TEM images represent 100 nm.

thickness of the phosphor shell. Shell thickness-dependent up-converted UV emission intensity enhancement for the $_{40}$Ag@YSO:Pr^{3+} PYSNPs is presented in **Figure 6**. As expected, the emission intensity of the up-converted UV light in the Ag@Void@YSO:Pr^{3+} PYSNPs is stronger than that of the pristine hollow YSO:Pr^{3+} phosphor, highlighting the contribution of the plasmon-assisted up-conversion process. Figure 6 shows the emission spectra and TEM images of the $_{40}$Ag@YSO:Pr^{3+} yolk-shell nanostructures with different phosphor shell thicknesses. All these nanostructures are of 220 ± 20 nm final sizes with inner hollow space diameter of 60 ± 25 nm. Compared with the pristine hollow YSO:Pr^{3+} structures (without Ag core), all the $_{40}$Ag@YSO:Pr^{3+} yolk-shell structures with 25, 40, 50, and 80 nm thick phosphor layers revealed enhanced UV emission. The increase in up-converted UV emission intensity in the hybrid nanophosphors were estimated to be about 21.9%, 45.1%, 48.4%, and 23.7%, respectively. The geometrical structures utilized for the study are summarized in Table S1, Supporting information. The lower emission enhancement for the $_{40}$Ag@YSO:Pr^{3+} nanostructures of 80 nm shell thickness is due to their thicker phosphor shells, which reduces the transmission of exciting photons to the plasmonic Ag core, reducing the effect of plasmon-assisted up-conversion process. On the other hand, in the PYSNPs of thinner shells, the intensity of up-converted UV emission through the direct up-conversion process is low, due to shorter path length (thinner shell thickness) of the exciting visible light for the up-conversion.

As the emission intensity in a phosphor material is proportional to the number of emitted photons, we estimated the emission enhancement in the Ag@YSO:Pr^{3+} nanophosphors by calculating the area under their emission curves in-between 260 and 360 nm spectral range and subtracting the area under

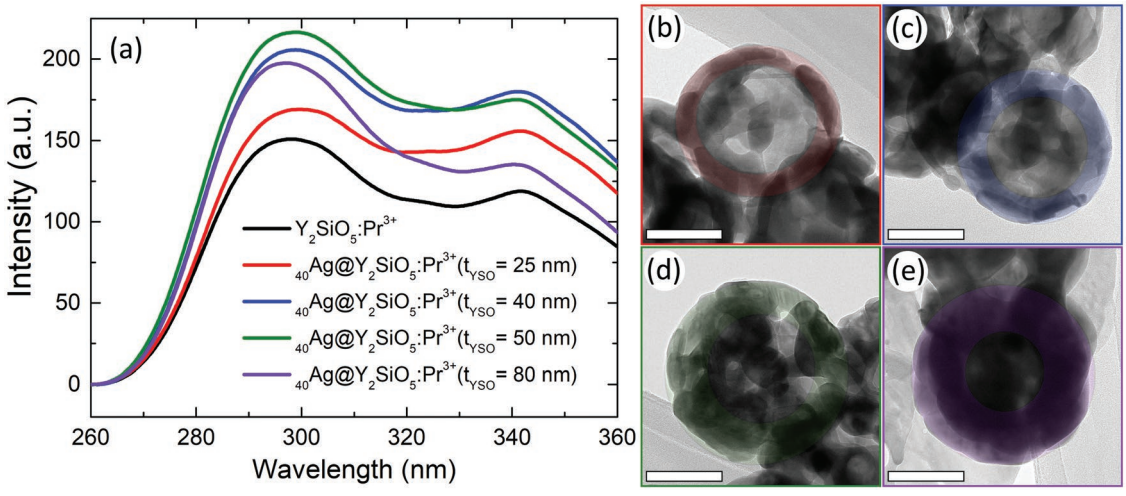

Figure 6. a) Emission spectra at 488 nm excitation, and TEM images of $_{40}$Ag@YSO:Pr^{3+} yolk-shell nanostructure of different shell thickness: b) 25 nm (red), c) 40 nm (blue), d) 50 nm (green), and e) 80 nm (violet) of shell thickness. YSO shells have been highlighted with their respective colors, to facilitate identification. White bars in TEM images represent 100 nm.

the emission curve of the pristine hollow YSO:Pr^{3+} nanophosphor (Figure 4). For both cases, the background associated to scattering and other non-associated optical processes was subtracted, taking as reference the emission spectra of the YSO nanostructures without Pr^{3+} ions. The areas under the considered range (260–360 nm) of the emission spectra of YSO:Pr^{3+} and $_{40}$Ag@YSO:Pr^{3+} sample of 50 nm shell thickness (≈200 nm final size) were estimated to be of 6864 and 12 812 a.u., respectively; which indicate about 86.7% enhancement in the UV up-conversion efficiency of the PYSNP with respect to YSO:Pr^{3+}.

Quantum efficiency (QE) of the up-conversion process can be calculated using the equation:[34]

$$QE = \frac{E}{A} \tag{6}$$

where E and A are the number of photons emitted and absorbed, respectively. To estimate the number of absorbed photons, we calculated the area under the excitation spectra of a reference aluminum sample with high reflectance, fixing the wavelength (488 nm) and width of emission and excitation slits of the spectrophotometer (Figure S17a, Supporting Information). Then, the number of absorbed photons was estimated by multiplying the area under the excitation band (A_{Ex}, Figure S17a, Supporting Information) with the absorbance of the nanophosphor powder film at 488 nm (Figure S17b, Supporting Information). Hence, the quantum efficiency of the powder films for our configuration is:

$$QE = \frac{E}{A_{Ex} \times A} \tag{7}$$

The calculated QE for the pristine hollow YSO:Pr^{3+} and $_{40}$Ag@YSO:Pr^{3+} nanophosphors (see Supporting Information) were 12.6% and 37.8%, respectively, indicating about 200% QE enhancement in the PYSNPs, due to the introduction of plasmonic Ag core.

2.2. Test of Prototype Smart Window

Figure 7 presents the schematic illustration of the up-conversion process occurred in the plasmon-mediated yolk-shell

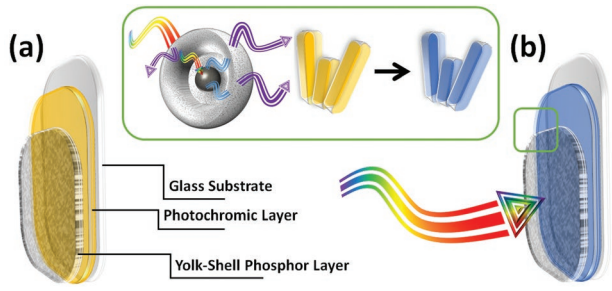

Figure 7. Schematic illustration of up-conversion layer approach using plasmon-mediated yolk-shell nanophosphor for photochromic application. In the PC/PYSNP double layer film, the original yellowish PC layer (a) is changed to blue color (b) when absorbing UV light, due to the photochromic reaction (inset).

nanophosphors. For fabricating a prototype smart window, PC WO_3 layers of about 9.0 µm thickness were prepared through doctor blading of prefabricated WO_3 nanorods (octagonal, PDF # 33–1387, Figure S18, Supporting Information) over window glass (3.5 cm × 3.5 cm) substrates. $_{40}$Ag@YSO:Pr^{3+} PYSNP layers of different thicknesses (2.0, 8.0, and 25.0 mm; Figure S19, Supporting Information) were then spin coated over the PC layers.

Fabricated $WO_3/_{40}$Ag@YSO:Pr^{3+} double-layer films were irradiated with one Sun simulated solar light, to analyse the kinetics of photochromic conversion. Optical absorption spectra of the fabricated double-layer films were recorded after 0, 10, 30, 60, 90, and 120 min (Figure S20, Supporting Information). Visible light absorption intensity of the PC layer (without PYSNP layer) in 400–800 nm wavelength range increased with irradiation time due to the formation of $H_xW^{5+}{}_xW^{6+}{}_{1-x}O_3$ and its color changed from yellow to blue (Figure S21, Supporting Information).[35] Moreover, the color switching behavior of the composite $WO_3/_{40}$Ag@YSO:Pr^{3+} double-layer films did not change noticeably even after 3 cycling (Figure S22, Supporting Information). The coloration rate of the PC/PYSNP double-layer films was calculated by fitting the change of area under the absorption curve (with respect to the same sample before irradiation), in 400–800 nm range, (ΔA) as a function of irradiation time:

$$\Delta A = A_\infty \left[1 - e^{-bt}\right] \tag{8}$$

Then, the coloration rate in the corresponding film can be determined as the initial slope (when $t \to 0$) of the curve: $R = A_\infty \times b$ (dashed lines in **Figure 8**a). The coloration rates were determined to be 0.583 ± 0.387 a.u. for the reference PC film, and 0.636 ± 0.223, 5.537 ± 1.492, and 14.586 ± 3.359 a.u. for the PC/PYSNP double-layer films containing 2, 8, and 25 µm thick PYSNP layer, respectively. As can be noticed, the rate of photochromic reaction in the fabricated double-layer films enhanced by 9%, 849%, and 2400% (a 24-fold increase) with the introduction of 2, 8, and 25 µm thick PYSNP layer, respectively. However, on increasing the PYSNP layer thickness beyond 25 µm, the change in color of the WO_3 layer upon one Sun solar light irradiation could not be detected by naked eye.

The electron transfer kinetics associated to photochromic behavior of the fabricated double-layer films was studied by estimating first-order reaction rate constant (k) corresponding to the photochromic reaction (W^{6+} to W^{5+}) using the relation:

$$kt = \ln\left[\frac{(A_0 - A_\infty)}{(A_t - A_\infty)}\right] \tag{9}$$

where A_0 is the solar light absorbance of the PC films before irradiation, A_∞ is the absorbance of the PC films after a long exposure to solar light (photochromic color saturation point, extracted from the fit with Equation 8) and A_t is the absorbance at particular irradiation time.[20,36]

The average photochromic kinetic constant (k) was determined to be 0.238 ± 0.081 s^{-1} for the WO_3 film and 1.168 ± 0.403, 1.262 ± 0.623, and 2.448 ± 0.586 s^{-1} for the PC/PYSNP double-layer films with a thickness of 2, 8, and 25 µm

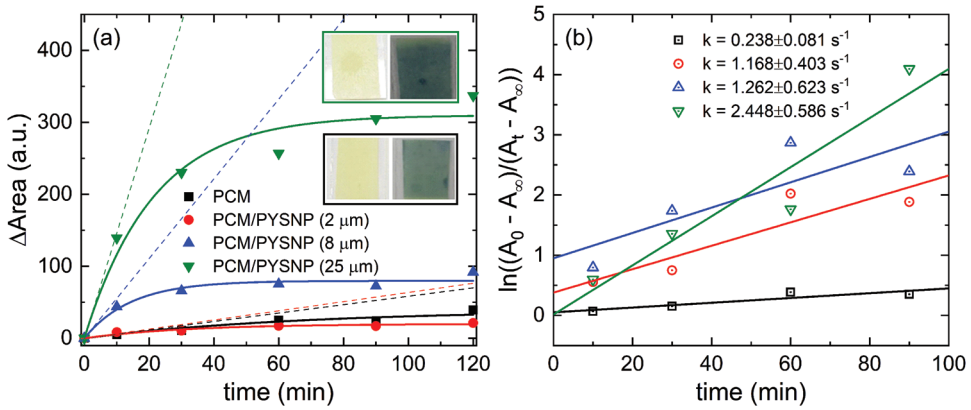

Figure 8. Determination of a) coloration rate and b) kinetic constants for plasmon-mediated yolk-shell phosphor deposited over a WO_3 photochromic layer of 9 μm thickness. Pristine WO_3 photochromic layer (black), and with 2 μm (red), 8 μm (blue), and 25 μm (green) thick plasmon-mediated yolk-shell phosphor layers. Continuous lines in (a) and (b) are, respectively, exponential and linear fits of the data. Dashed lines in (a) represent the slope of the curve, used to determine the coloration rate. Insets in (a) present the optical images, before and after one Sun solar irradiation, of single photochromic film (lower, black rectangle) and the double-layered film with PYSNP layer of 25 μm (upper, green rectangle). The data points in the graphs (both (a) and (b)) correspond to the average of at least 3 measurements performed on 3 samples of each set of films under the same experimental conditions. Error bars are not shown due to very small dispersion in data values.

in the PYSNP layer, respectively. This translates in an increase of the rate constant, k, with respect to the pristine PC WO_3 layer, of about 390%, 430%, and 980% for the 2, 8, and 25 μm PYSNP layer films. The UV light emitted by PYSNP layer due to up-conversion is responsible for the considerable improvements observed in the PC/PYSNP double-layer films. This additional UV radiation, together with the UV radiation in the solar spectrum, reaches the PC WO_3 layer, generating oxygen vacancies and photoelectrons, via the photochromic reaction, and forming $H_xW^{5+}{}_xW^{6+}{}_{1-x}O_3$ (Figure S21, Supporting Information). This explains why the coloration rate and the kinetic constant of photochromic reaction of WO_3 film were enhanced by about 24 and 10 times.

3. Conclusion

Using a three-step wet-chemical synthesis process, we fabricated geometry-optimized plasmonic yolk-shell nanophosphors Ag@Void@YSO:Pr^{3+} with high up-conversion ability. Geometrically-optimized PYSNP exhibited an emission efficiency almost 50% higher than that of YSO:Pr^{3+} phosphor shells. The enhanced up-conversion capacity of the hybrid composite nanophosphor is attributed to two up-conversion processes, one in the direct up-conversion associated to inter-band transition of Pr^{3+} ions due to the absorption of incident visible light, and the other is the plasmon-assisted up-conversion due to excitation through energy transfer by the plasmonic Ag nanocore particles, excited by the light transmitted through the phosphor shell layer. By applying these plasmonic yolk-shell nanophosphors at the front surface (illuminating face) of photochromic WO_3 films, their coloration rate and kinetic constant could be enhanced up to 24 and 10 times, respectively. The results presented in this work clearly demonstrate a pathway for fabricating photochromic smart windows of high quantum efficiency with swift color change, for utilizing in modern building systems.

4. Experimental Section

Materials: Silver (I) nitrate ($AgNO_3$, 99.8% Junsei Chemical), trisodium citrate dihydrate ($C_6H_5Na_3O_7{\cdot}2H_2O$, 99.9%, Junsei Chemicals), tannic acid ($C_{76}H_{52}O_{46}$, Aldrich), D-glucose ($C_6H_{12}O_6$, 98.0%, Katayama Chemical), yttrium(III) nitrate tetrahydrate ($Y(NO)_3{\cdot}4H_2O$, 99.99%, Aldrich), praseodymium(III) nitrate hexahydrate ($Pr(NO_3)_3{\cdot}6H_2O$, 99.9%, Aldrich), urea (NH_2CONH_2, 98.0%, Samchun Chemicals), tetraethyl orthosilicate ($(SiC_2H_5O)_4$, 98%, Samchun Chemicals), ammonia solution (28% Junsei Chemicals) were utilized for materials synthesis as received, without further purification. Polyvinylpyrrolidone (PVP Mw: 29000, Aldrich), sodium tungstate dihydrate ($Na_2WO_4{\cdot}2H_2O$, ≥ 99%, Sigma Aldrich), hydrochloric acid (HCl, 35 wt%), ethanol (C2H6O, ≥ 99.9%, Emsure), and deionized water (ρ>18 MΩ.cm, Millipore) were utilized in the reaction and washing process.

Solution-Based Synthesis of Ag Nanoparticles: Ag nanoparticles of 10 nm diameters were synthesized through the solution-based procedure reported by Bastús et al.,[28] with minor modification. In a typical synthesis, 0.735 g of trisodium citrate and 0.425 g of tannic acid were added into 100 mL of DI water in a 250 mL 3-necked round bottom flask coupled with glass condenser, under vigorous magnetic stirring for 20 min. The precursor solution was heated at 100 °C for 20 min, and 1 mL of aqueous 25 mM $AgNO_3$ solution was injected. The temperature of the reaction mixture was reduced to 90 °C, and the reaction was allowed to continue for a couple of minutes. After about 30 s of addition of the $AgNO_3$ solution, the color of the reaction mixture turned yellowish from slightly brown translucent, indicating the formation of Ag nanoparticles. The reactor was then cooled down to the room temperature using iced water for 15 min. The synthesized sample was denoted as $_{10}$Ag.

The as-synthesized colloidal $_{10}$Ag sample was taken as seed particles for the synthesis of $_{40}$Ag, $_{80}$Ag and $_{120}$Ag samples. For the synthesis of larger Ag particles, 20 mL of colloidal $_{10}$Ag sample was first dispersed in 20 mL of DI water and heated to 90 °C under magnetic stirring. Then 0.2 mL of 25 mM trisodium citrate, 0.2 mL of 2.5 mM tannic acid and 0.4 mL of 25 mM $AgNO_3$ solutions were sequentially injected at about 45 s intervals and reaction was continued at 90 °C for 20 min. The above-mentioned procedure was repeated for 8 times to obtain $_{40}$Ag sample. The samples obtained by repeating the procedure for 19 and 22 times were designated as $_{80}$Ag and $_{120}$Ag, respectively. Expected average size of the Ag nanoparticles in the samples of $_{10}$Ag, $_{40}$Ag, $_{80}$Ag, and $_{120}$Ag were determined as 10, 40, 80, and 120 nm, respectively.

Fabrication of Ag@C@Y(OH)CO_3:Pr^{3+}@SiO_2 Structures and Yolk-Shell Ag@YSO:Pr^{3+} Nanophosphors: For the fabrication of Ag@C

core-shell structures, ≈1 mL of 0.047 M Ag nanoparticle solution was dispersed in 20 mL of DI water. 1.5 g of D-glucose was added to the Ag solution under vigorous magnetic stirring for 15 min. The resulted mixture was transferred into a 20 mL Teflon-lined autoclave and heated at 180 °C for 0.5, 1, 2, or 3 h for hollow void of 60, 120, 160, and 240 nm, respectively. On completing the hydrothermal reaction, the autoclave was rapidly cooled down to room temperature by immersing in cold water. Carbon coated Ag nanocore, Ag@C were separated and washed in DI water several times by centrifugation and dried overnight at 60 °C. For the fabrication of Ag@C@Y(OH)CO_3:Pr^{3+} structures, 0.05 g of Ag@C nanoparticles were dispersed in 25 mL of DI water under ultrasonication for 1 h. 0.33 g of $Y(NO_3)_3$•$6H_2O$, 3.0 g of urea, and 0.01 g of $Pr(NO_3)_3$•$6H_2O$ were added to the Ag@C dispersed solution under magnetic stirring for 30 min. After heating the mixture solution at 90 °C for 2 h, the product was washed with DI water, collected by centrifugation and dried overnight at 60 °C. About 0.05 g of Ag@C@Y(OH)CO_3:Pr^{3+} particles were dispersed in 25 mL of ethanol under ultrasonication. For SiO_2 coating, TEOS and 1.45 mL of ammonia solution (30 wt%) were added to the colloidal solution under magnetic stirring for 2 h at room temperature. A phosphor thickness of 25, 40, 50, and 80 nm was obtained by adding 0.03, 0.04, 0.05, and 0.06 mL of TEOS. The SiO_2 coated Ag@C@Y(OH)CO_3:Pr^{3+} particles were collected by centrifugation, washed two times by ethanol, and dried at 60 °C for 2 h. The dried Ag@C@Y(OH)CO_3:Pr^{3+}@SiO_2 particles were calcinated at 1000 °C in air for 3 h in a box furnace at 2 °C min^{-1} heating rate for the formation of yolk-shell nanophosphor of Ag@YSO:Pr^{3+}.

Fabrication of Double-Layer Ag@YSO:Pr^{3+}/WO_3 Films: In a typical synthesis of WO_3 nanoparticles of octagonal phase, a 30 mL aqueous solution (0.2 M) of Na_2WO_4•$2H_2O$ was added to 0.025 g of PVP (Mw: 29 000) dissolved in 10 mL of DI water under vigorous stirring for 15 min. The mixture solution was heated at 90 °C for 10 min in a hot water bath under agitation. After that, 7.8 mL of 3 M HCl solution was added to the mixture and the reaction was continued at this temperature (90 °C) for 3 h. The reaction pot was cooled down to room temperature and the formed product was separated, washed with water-ethanol (1:1) mixture three times through centrifugation, and dried at 60 °C for 3 h.

To fabricate the photochromic WO_3 films, a dense colloidal suspension was prepared by dispersing 0.2 g of WO_3 in a mixed solvent containing 5 mL of DI water, 0.2 mL of glacial acetic acid, and 2.5 mL of ethylene glycol. The suspension was kept under vigorous magnetic stirring for two days at 90 °C, until about half of the solvent was evaporated. The dense WO_3 suspension was utilized to fabricate photochromic films, by doctor blading technique, over glass substrates treated with O_2 plasma (for 1 min). The as-prepared films were air-dried for 3 h. For the fabrication of plasmonic phosphor layer over the photochromic films, a dense colloidal suspension of the Ag@YSO:Pr^{3+} nanophosphor was prepared by the same process utilized for WO_3 suspension. The Ag@YSO:Pr^{3+} suspension was spin-coated over the WO_3 layer deposited glass substrates at 1000 rpm revolution for 60 s, and dried in air for 3 h.

Characterization: Crystal structure of the final Ag@YSO:Pr^{3+} nanophosphors was analyzed by XRD (Rigaku MiniFlex- II desktop X-ray diffractometer, Cu Kα radiation, λ = 1.5406 Å). Morphology and size of the phosphor particles were analyzed in a Hitachi S-4300 field-emission scanning electron microscope and JEOL JEM-2100F TEM, operated at 200 kV. Emission spectra of the Ag@YSO:Pr^{3+} phosphor particles (in powder form) were recorded in a Hitachi F-700 fluorescence spectrophotometer, under 488 nm excitation from a Xenon lamp. Optical spectra of the nanophosphors, WO_3 films, and double-layer Ag@YSO:Pr^{3+}/WO_3 films were recorded in a Varian Cary 5000 UV–vis–NIR spectrophotometer (Agilent Technologies). The kinetic function of the PYSNP film over PC layer was investigated using solar simulated light source (Asahi HAL-320, 100 mW cm^{-2}). Solar light of one Sun intensity from the solar simulator was irradiated over about 11 cm^2 area of the double-layer composite films for different durations. All the data points were obtained by averaging experimental results over three samples of each set.

Finite Differences in the Time Domain Simulation: Optical response of yolk-shell structures was calculated using the FDTD method,[37] as implemented in the free software package MEEP.[38] Maxwell equations are solved in this method by a second order approximation, dividing the space into a discrete grid, the Yee grid,[39] and evolving the fields in time with discrete time steps. A schematic representation of the geometry used for the calculation is shown in Figure S13, Supporting Information. Simulations were performed using a spatial resolution of 1 nm. For eccentric cores, the calculation was performed twice, for the polarizations parallel and perpendicular to the displacement axis.

Supporting Information

Supporting Information is available from the Wiley Online Library or from the author.

Acknowledgements

This work was supported by the Leader Project at the Korea Institute of Energy Technology (KENTECH), funded by the Ministry of Science and ICT, through the National Research Foundation of Korea (No. 2020R1A3B3079715). U.P. acknowledges CONACyT, Mexico, for funding through the grant # CB 2017-2018/A1-S-26720. O.P.-R. acknowledges the computer resources and technical assistance provided by the Centro de Supercomputación y Visualización de Madrid (CeSViMa).

Conflict of Interest

The authors declare no conflict of interest.

Author Contributions

C.W.K wrote original draft, analyzed, and interpreted the results. E.G.S. conducted the experiments and analyzed the results. A.U.P. participated in experiments and analysis of results. D.K.L. revised original draft. O.P.-R. performed the theoretical calculations and analyzed the results. U.P. participated in experiments and analysis of results. Y.S.K. designed and supervised the research. The manuscript was reviewed through contributions of all authors. All authors have given approval to the final version of the manuscript.

Data Availability Statement

Research data are not shared.

Keywords

nanophosphors, near-field controlled up-conversion enhancement, smart windows, yolk-shell nanoparticles

Received: September 22, 2022
Revised: November 13, 2022
Published online:

[1] U. Berardi, *Resour., Conserv. Recycl.* **2017**, *123*, 230.
[2] Y. Ke, J. Chen, G. Lin, S. Wang, Y. Zhou, J. Yin, P. S. Lee, Y. Long, *Adv. Energy Mater.* **2019**, *9*, 1902066.

[3] Y. Ke, C. Zhou, Y. Zhou, S. Wang, S. H. Chan, Y. Long, *Adv. Funct. Mater.* **2018**, *28*, 1800113.
[4] Y. Wang, E. L. Runnerstrom, D. J. Milliron, *Annu. Rev. Chem. Biomol. Eng.* **2016**, *7*, 283.
[5] G. Cai, J. Wang, P. S. Lee, *Acc. Chem. Res.* **2016**, *49*, 1469.
[6] C. J. Barile, D. J. Slotcavage, J. Hou, M. T. Strand, T. S. Hernandez, M. D. McGehee, *Joule* **2017**, *1*, 133.
[7] J. A. H. P. Sol, G. H. Timmermans, A. J. van Breugel, A. P. H. J. Schenning, M. G. Debije, *Adv. Ener. Mater.* **2018**, *8*, 1702922.
[8] E. P. A. van Heeswijk, J. J. H. Kloos, N. Grossiord, A. P. H. J. Schenning, *J. Mater. Chem. A* **2019**, *7*, 6113.
[9] H. Khandelwal, A. P. H. J. Schenning, M. G. Debije, *Adv. Energy Mater.* **2017**, *7*, 1602209.
[10] B. R. Park, J. Hong, E. J. Choi, Y. J. Choi, C. Lee, J. W. Moon, *Energies* **2019**, *12*, 1181.
[11] L. Long, H. Ye, *Sci. Rep.* **2014**, *4*, 6427.
[12] N. C. Davy, M. Sezen-Edmonds, J. Gao, X. Lin, A. Liu, N. Yao, A. Kahn, Y.-L. Loo, *Nat. Energy* **2017**, *2*, 17104.
[13] A. Llordés, G. Garcia, J. Gazquez, D. J. Milliron, *Nature* **2013**, *500*, 323.
[14] H. Kim, Y. Kim, K. S. Kim, H. Y. Jeong, A.-R. Jang, S. H. Han, D. H. Yoon, K. S. Suh, H. S. Shin, T. Y. Kim, W. S. Yang, *ACS Nano* **2013**, *7*, 5769.
[15] B. Jiang, L. Liu, Z. Gao, W. Wang, *Adv. Opt. Mater.* **2018**, *6*, 1800195.
[16] M. Irie, T. Fukaminato, K. Matsuda, S. Kobatake, *Chem. Rev.* **2014**, *114*, 12174.
[17] E. Orgiu, P. Samorì, *Adv. Mater.* **2014**, *26*, 1827.
[18] E. P. Ferreira-Neto, S. Ullah, F. L. S. de Carvalho, A. L. de Souza, M. Oliveira Jr., J. F. Schneider, Y. P. Mascarenhas, A. M. Jorge Jr., U. P. Rodrigues-Filho, *Mater. Chem. Phys.* **2015**, *153*, 410.
[19] R. Pardo, M. Zayat, D. Levy, *Chem. Soc. Rev.* **2011**, *40*, 672.
[20] M. J. Kang, E. G. Santoro, Y. S. Kang, *ACS Omega* **2018**, *3*, 9505.
[21] W. Feng, T. R. Zhang, Y. Liu, R. Lu, Y. Y. Zhao, J. N. Yao, *J. Mater. Sci.* **2003**, *38*, 1045.
[22] T. Yamase, *Chem. Rev.* **1998**, *98*, 307.
[23] N. I. Gumerova, A. Rompel, *Nat. Rev. Chem.* **2018**, *2*, 0112.
[24] C. W. Kim, T. Y. Eom, I. S. Yang, B. S. Kim, W. I. Lee, Y. S. Kang, Y. S. Kang, *Sci. Rep.* **2017**, *7*, 6849.
[25] C. W. Kim, D. K. Kim, W. J. Shin, M. J. Choi, Y. S. Kang, Y. S. Kang, *Nano Energy* **2015**, *13*, 573.
[26] S. Wang, W. Gao, X.-Y. Hu, Y.-Z. Shen, L. Wang, *Chem. Commun.* **2019**, *55*, 4137.
[27] T.-C. Chang, X. Cao, S.-H. Bao, S.-D. Ji, H.-J. Luo, P. Jin, *Adv. Manuf.* **2018**, *6*, 1.
[28] N. G. Bastús, F. Merkoçi, J. Piella, V. Puntes, *Chem. Mater.* **2014**, *26*, 2836.
[29] M. D. Susman, A. Vaskevich, I. Rubinstein, *J. Phys. Chem. C* **2016**, *120*, 16140.
[30] P. Yuan, Y. H. Lee, M. K. Gnanasammandhan, Z. Guan, Y. Zhang, Q.-H. Xu, *Nanoscale* **2012**, *4*, 5132.
[31] P. Bharadwaj, L. Novotny, *Opt. Express* **2007**, *15*, 14266.
[32] P. B. Johnson, R. W. Christy, *Phys. Rev. B* **1972**, *6*, 4370.
[33] X. Qin, X. Liu, W. Huang, M. Bettinelli, X. Liu, *Chem. Rev.* **2017**, *117*, 4488.
[34] A. P. Jadhav, A. U. Pawar, U. Pal, Y. S. Kang, *J. Mater. Chem. C* **2013**, *2*, 496.
[35] S. Wang, W. Fan, Z. Liu, A. Yu, X. Jiang, *J. Mater. Chem. C* **2018**, *6*, 191.
[36] J. Wang, S.-L. Li, X.-M. Zhang, *ACS Appl. Mater. Interfaces* **2016**, *8*, 24862.
[37] A. Taflove, *IEEE Trans. Electron. Comput.* **1980**, *22*, 191.
[38] A. F. Oskooi, D. Roundy, M. Ibanescu, P. Bermel, J. D. Joannopoulos, S. G. Johnson, *Comput. Phys. Commun.* **2010**, *181*, 687.
[39] K. Yee, *IEEE Trans. Antennas Propag.* **1966**, *14*, 302.